Steering and Encoding the Polarization of Second Harmonic in the Visible with a Monolithic $LiNbO_3$ Metasurface

Luca Carletti,[†,‖] Attilio Zilli,[‡,‖] Fabio Moia,[¶] Andrea Toma,[¶] Marco Finazzi,[‡] Costantino De Angelis,[†] Dragomir N. Neshev,[*,§] and Michele Celebrano[*,‡]

†*Department of Information Engineering, University of Brescia, Via Branze 38, Brescia 25123, Italy*

‡*Politecnico di Milano, Physics Department, Piazza Leonardo da Vinci 32, 20133 Milano, Italy*

¶*Istituto Italiano di Tecnologia, Via Morego 30, 16163 Genova, Italy*

§*ARC Centre of Excellence for Transformative Meta-Optical Systems (TMOS), Research School of Physics, Australian National University, 58 Mills Rd, Acton ACT 2601, Australia*

‖*These authors contributed in equal measure to this work*

E-mail: dragomir.neshev@anu.edu.au; michele.celebrano@polimi.it

Abstract

Nonlinear metasurfaces constitute a key asset in meta-optics, given their ability to scale down nonlinear optics to sub-µm thicknesses. To date, nonlinear metasurfaces have been mainly realized using narrow band-gap semiconductors, with operation limited to the near-infrared range. Nonlinear meta-optics in the visible range can be realized using transparent materials with high refractive index, such as lithium niobate ($LiNbO_3$). Yet, efficient operation in this strategic spectral window has been so far prevented by the nanofabrication challenges associated with $LiNbO_3$, which considerably limit the aspect ratio and minimum size of the nanostructures (*i. e.* meta-atoms). Here we demonstrate the first monolithic nonlinear periodic metasurface based on $LiNbO_3$ and operating in the visible range. Realized through ion beam milling, our metasurface features a second-harmonic (SH) conversion efficiency 2.4×10^{-8} at a pump intensity as low as $0.5\,\mathrm{GW/cm^2}$. By tuning the pump polarization, we demonstrate efficient steering and polarization encoding into narrow SH diffraction orders, opening novel opportunities for polarization-encoded nonlinear meta-optics.

Keywords

Nonlinear nanophotonics, nonlinear diffraction, lithium niobate, metasurface, second-harmonic generation

The interest in nonlinear nanophotonics based on dielectric materials has been rising fast during the last decade.[1–3] The employment of materials with high refractive index and large nonlinear susceptibility along with low absorption in the near infra-red (NIR), fostered the enhancement of nonlinear effects at the nanoscale to unprecedented levels in this wavelength range.[4–10] Metasurfaces composed by ensembles of dielectric nanoresonators with sub-wavelength dimensions – *i. e.* meta-atoms – have been employed to enhance[11,12] and control[10,13–15] the nonlinearly generated light, providing new tools for ultra-compact nonlinear meta-optics. Thus far, nonlinear metasurfaces have been applied to the generation of either third-harmonic (TH) or second-harmonic (SH), depending on the meta-atom material composition. Group IV semiconductors have been used for third-harmonic generation (THG)[12,14,15], whereas III–V semiconducting compounds and alloys have been used for second-harmonic generation (SHG)[11,13,16]. The choice of these materials is mainly driven by the availability of state-of-the-art nanofabrication technologies for CMOS-compatible platforms.[1] Nonetheless, most semiconductors feature narrow band-gaps, with onsets of the optical absorption in the NIR wavelength range.[6,7,13] This has hindered thus far the development of low-loss nonlinear meta-optics at visible wavelengths.

Lithium niobate ($LiNbO_3$) is a material with a wide transparency window spanning from the ultraviolet to the mid-infrared, which enables operation in the visible (VIS) spectral range. $LiNbO_3$ features a moderately high refractive index and a sizable second-order optical nonlinear response. These unique properties, which make $LiNbO_3$ one of the the most widely employed materials in nonlinear photonics and electro-optics, motivated the recent efforts towards the realization of $LiNbO_3$-based nanostructures[17–19] and metasurfaces.[20–25] Yet, the realization of monolithic $LiNbO_3$ metasurfaces has been hindered by the complexity of the nanofabrication processes. In particular, electron-beam lithography (EBL) combined with Ar^+-based reactive ion etching – a commonly employed technique to realize $LiNbO_3$-based integrated photonics circuits[26,27] – limits the realization of nanostructures with a high aspect ratio, which is crucial to enhance field confinement and cavity effects in the VIS range.

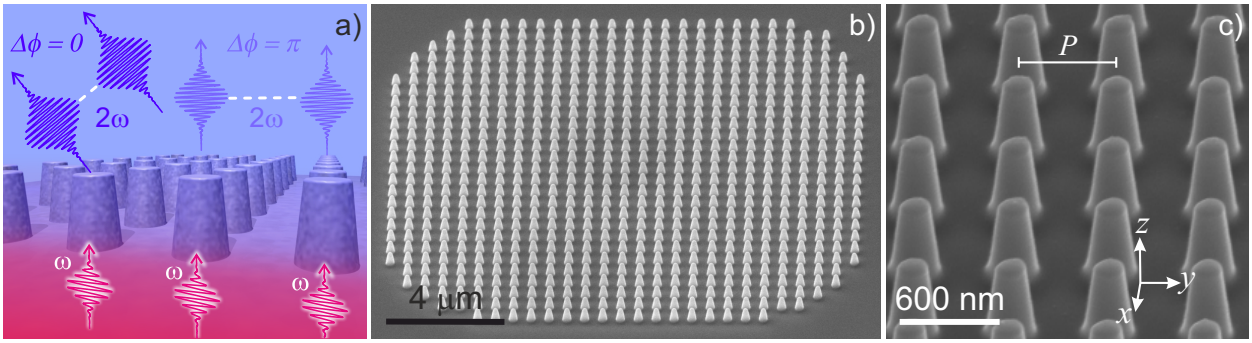

Figure 1: $LiNbO_3$ metasurface operating principle and geometry. a) Sketch of the diffraction mechanism at play in the metasurfaces. The pump at angular frequency ω impinges on the $LiNbO_3$ nanopillar grating from the substrate side. The SH, generated at angular frequency 2ω, is removed from the zeroth diffraction order and directed to the first diffraction orders thanks to the interference between the emission patterns of the individual nanopillars. b) Electron microscopy image of one of the realized metasurfaces of diameter 15 µm. c) Zoom of the nanopillars showing a ∼80° side-wall inclination and a flat top obtained at the end of the process. The base radius of each nanopillar is 175 nm, the height is 420 nm and the array pitch, P, is 590 nm. The metasurface lies in the xy Cartesian plane, with the extraordinary axis of $LiNbO_3$ along z.

Focused ion beam (FIB) milling, on the other hand, allows to fabricate nanostructures with high aspect ratio and steep side walls, which is essential to deploy the full potential of $LiNbO_3$-based nanostructures and metasurfaces. This approach has been recently applied to realize $LiNbO_3$-based metasurfaces limited to a 1D periodicity.[20,23]

In this work, we realize a monolithic $LiNbO_3$ nonlinear metasurface from a z-cut $LiNbO_3$ thin film and characterize its ability to up-convert NIR light to the VIS range via SHG. Periodic metasurfaces, such as the one reported here, provide multiple degrees of freedom for engineering the properties of the emitted nonlinear light. In particular, (i) the lattice periodicity allows steering the emitted light into narrow diffraction orders, (ii) the geometry of the individual meta-atom along with its crystalline orientation and lattice structure enables one to engineer the polarization state of the emitted light based on that of the excitation light.[13] In addition, (iii) the design of the meta-atoms governs the local amplitude and phase of the emitted light, which can be employed to shape the wave-front of the nonlinear emitted light.[10,14,15,28,29] In our metasurface the SHG process is driven by a magnetic dipole (MD) resonance at the fundamental wavelength (FW) in each individual meta-atom, which

efficiently couples to the in-plane field components of a linearly polarized beam impinging at normal incidence. Energy conversion to the SH is promoted by the out-of-plane component of the nonlinear polarization, while the interference between higher order multipoles in the meta-atom at the SH wavelength along with the lattice periodicity enables the efficient emission of the SH into diffraction orders (see Figure 1a). This mechanism also allows to encode the polarization of the pump beam into specific SH polarization states and specific diffraction orders. Our experimental results are in excellent agreement with the numerical simulations employed to design the metasurfaces[22], providing a full description of both the linear and nonlinear optical processes at work.

The samples are realized on commercially-available z-cut $LiNbO_3$ films grown on a transparent quartz substrate (NanoLN – Jinan Jingzheng Electronics Co.). The metasurfaces are obtained by directly milling the 5 µm-thick $LiNbO_3$ film by FIB (FEI - Dual Beam Helios Nanolab 650). A detailed description of the fabrication process is presented in Section S.II of the supporting information (SI). Briefly, Ga^+ ions are emitted with a current of 230 pA and accelerated by a voltage of 30 keV. The overall ion dose is optimized to achieve a patterning depth of around 420 nm. To avoid charging effects, a 200 nm thick Cr layer is deposited by radio-frequency sputtering before the ion milling and then removed in standard chrome etch solution (micro resist technology GmbH). The Cr film acts also as a sacrificial layer to prevent further alterations induced by Ga^+ ions on the top surface of the $LiNbO_3$ pillars during the milling process. Figure 1b shows a scanning electron microscopy image of the realized metasurface, which spans an area of about 15 µm × 15 µm with an array pitch, P, of 590 nm, and a nanopillar radius of $R = 175$ nm (Figure 1b and c). To design such optimized geometry, similarly to Ref. 22, we employed full-vectorial numerical simulations that are described in the SI. The FIB technique allowed attaining an angle of the side walls of the nanopillars that is 83.6°, see Figure 1c. It is worth noting that, since the pump beam propagates along the extraordinary axis (z-cut), the SHG process is highly inefficient in the $LiNbO_3$ film.[22] Therefore, the SHG enhancement is mainly driven by the optical resonances

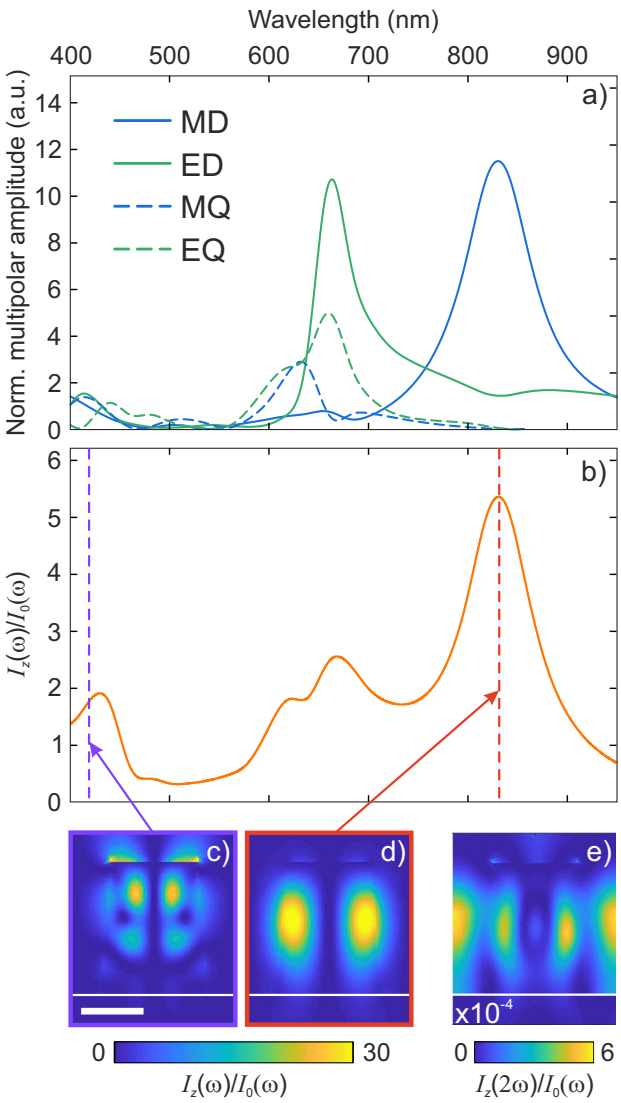

Figure 2: Multipolar decomposition. a) The blue lines represent the scattering contribution of the magnetic dipole (MD, solid) and of the magnetic quadrupole (MQ, dashed) modes, while the green lines of the electric dipole (ED, solid) and of the electric quadrupole (EQ, dashed) modes. b) Intensity enhancement averaged in the meta-atom volume. The metasurface parameters are $R = 175\,\text{nm}$ and $P = 590\,\text{nm}$. c,d) Intensity enhancements for the z-component in the meta-atom at 415 nm (c, violet frame) and 830 nm (d, red frame). The violet and red dashed vertical lines in (b) indicate the wavelength corresponding to the maps (c) and (d), respectively. e) Simulated SH intensity normalized to the incident one.

of the metasurface.

Figure 2a shows the Cartesian multipolar decomposition of the resonances that underpin the optical response of the optimized metasurface[30]. The marked MD resonance around 830 nm is responsible for the enhanced light–matter interaction in the nanopillars at the

FW. Concurrently, the magnetic quadrupole (MQ) and electric dipole (ED) resonances in the structure around 415 nm contribute to the efficient conversion of the impinging light into SH and its re-emission to the far field. Considering the z-cut wafer employed to realize the metasurface, the largest component of the induced nonlinear polarization density, $\mathbf{P}^{\mathrm{SH}}$, is P_z^{SH} since d_{33} is about one order of magnitude larger than the other nonlinear tensor elements, see section S.V of the SI. Therefore, E_z is expected to be the most relevant field component, both at the FW and at the SH. The E_z intensity enhancement in the nanopillar, shown in Figure 2b, features two peaks that overlap with either the FW or the SH. In particular, the peak at the FW stems from the MD resonance, confirming its key role in the SHG enhancement process. Conversely, the peak at SH wavelength features the superposition between an ED and a MQ resonance, which plays a key role in the polarized emission of the SH (see below and SI). The corresponding field intensity distribution maps inside the meta-atom at the FW and SH are shown in Figure 2c and d, respectively. Concurrently, the calculated SH field distribution (see Fig. 2e) indicate a favourable SH emission towards higher collection angles, which can be efficiently overlapped in the k-space to the first order diffraction of the metasurface.

Before assessing the nonlinear performances of the optimized metasurface, we compared the simulated linear transmittance of the structure with the measured one. Figure 3a shows the simulated transmittance spectra in the VIS–NIR range for three metasurfaces with $P =$ 590 nm. In the NIR, all spectra exhibit a transmittance increasing with the wavelength at correspondence with the MD resonance (see Fig. 2a). By comparing the transmittance of the optimized metasurface ($R = 175$ nm) against the other structures ($R = 150$ nm and 200 nm), one can verify that larger radii lead to a broadening of the extinction range and to a red-shift towards the NIR. Figure 3b shows the measured transmittance spectra for the metasurfaces simulated in Figure 3a. The spectra were recorded by focusing an incoherent white light from a tungsten lamp on the metasurfaces and coupling the transmitted light to a VIS–NIR spectrometer (Andor Shamrock 303 + iKON-M934 CCD Camera, Oxford

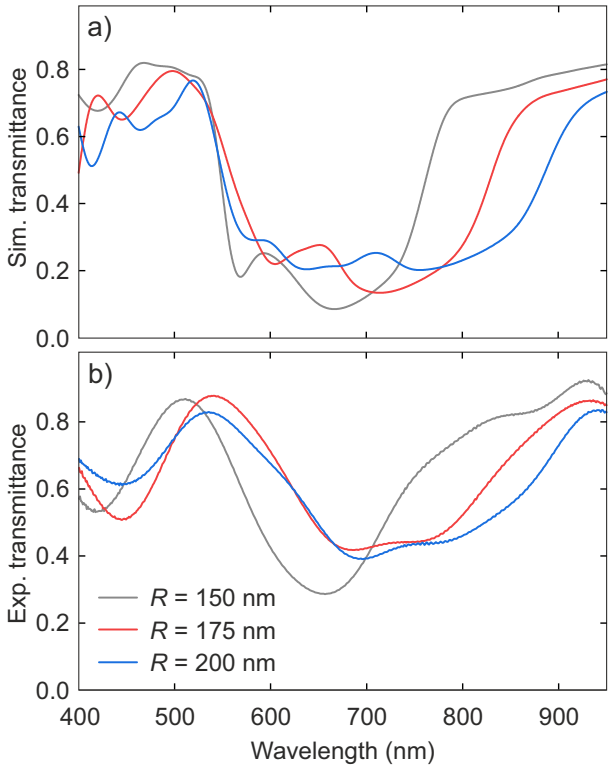

Figure 3: Linear transmittance. a) Simulated transmittance spectra of $LiNbO_3$ metasurfaces as a function of the meta-atom radius R as indicated by the shared legend in panel c. b) Measured transmittance spectra of the metasurfaces simulated in (a).

Instruments). The transmitted light from the unpatterned $LiNbO_3$ substrate was used as reference. The agreement between simulated (Figure 3a) and measured (Figure 3b) spectra demonstrate the quality of the nanofabrication process.

To characterize the SH emission properties of the metasurface, we employed a home-built nonlinear inverted microscope described in detail in Section S.I of the SI. Briefly, the sample was mounted with the metasurface facing the objective, while the excitation came from the $LiNbO_3$ substrate side, by loosely focusing the beam with a 60 mm focal length lens. This produced a 15 µm wide (FWHM) excitation spot, matching the lateral size of the metasurface. We employed excitation average powers up to 10 mW ($\sim$ 0.5 GW/cm^2 peak intensity), delivered by a tunable (680 nm to 1080 nm) Ti-sapphire laser (Chameleon Ultra II, Coherent Inc.), yielding 140 fs pulses at 80 MHz repetition rate. The emitted SH radiation was collected using a 0.85 numerical aperture (NA) objective, which corresponds

to a maximum collection angle of about 58°, and the back focal plane (BFP) of the objective was imaged by a CCD camera (see details in the SI). As the metasurface periodicity is larger than the SH wavelength, the first diffraction orders are expected at

$$\mathrm{NA}_1 = \frac{\lambda_{\mathrm{SH}}}{P} = \frac{415\,\mathrm{nm}}{590\,\mathrm{nm}} = 0.70\,\mathrm{NA} \tag{1}$$

corresponding to an angle of 44.7°. Figures 4a,b show exemplary BFP SHG images recorded using horizontal and vertical input polarization, respectively. Narrow emission spots (see bottom-left insets) appear at 0.70 NA as expected. In particular, the diffraction orders co-polarized with the FW beam are about 4 times more intense than the cross-polarized ones, which is in good agreement with the simulations (see insets in Figures 4c,d). The BFP images recorded on the unpatterned $LiNbO_3$, shown in Figures 4c and 4d, highlight that the intensity of the (0,0) diffraction order is insensitive to the polarization of the excitation beam. By comparing the BFP SHG images acquired on the metasurface with those on the unpatterned $LiNbO_3$ substrate one can readily notice a one order of magnitude suppression of the (0,0) diffraction order in the metasurface. This efficient diffraction is ascribed to the choice of z-cut $LiNbO_3$ substrate for the realization of our nonlinear metasurfaces. The BFP SHG maps were obtained by chromatically filtering the transmitted FW, see section S.I of the SI. This is confirmed by the collected emission spectra in Figure 4e, which show the presence of the sole SH peak centered at 412.5 nm when a FW of 825 nm is employed. To further verify the SH nature of the signal, we acquired power-dependent curves for each individual diffraction order. Figure 4f shows the SH conversion efficiency, $\eta \equiv P_{\mathrm{avg}}^{\mathrm{SH}}/P_{\mathrm{avg}}^{\mathrm{FW}}$, as a function of the the excitation power and peak intensity, where $P_{\mathrm{avg}}^{\mathrm{SH}}$ indicates the SH power emitted – once the detection efficiency of the experimental setup are accounted for (see the SI for details) – and $P_{\mathrm{avg}}^{\mathrm{FW}}$ is the excitation power. As expected, the dependence of η on the excitation power or peak intensity is linear, given that the system operates in the undepleted pump regime. The power curves in Figure 4f together with the emission spectra in Figure 4e

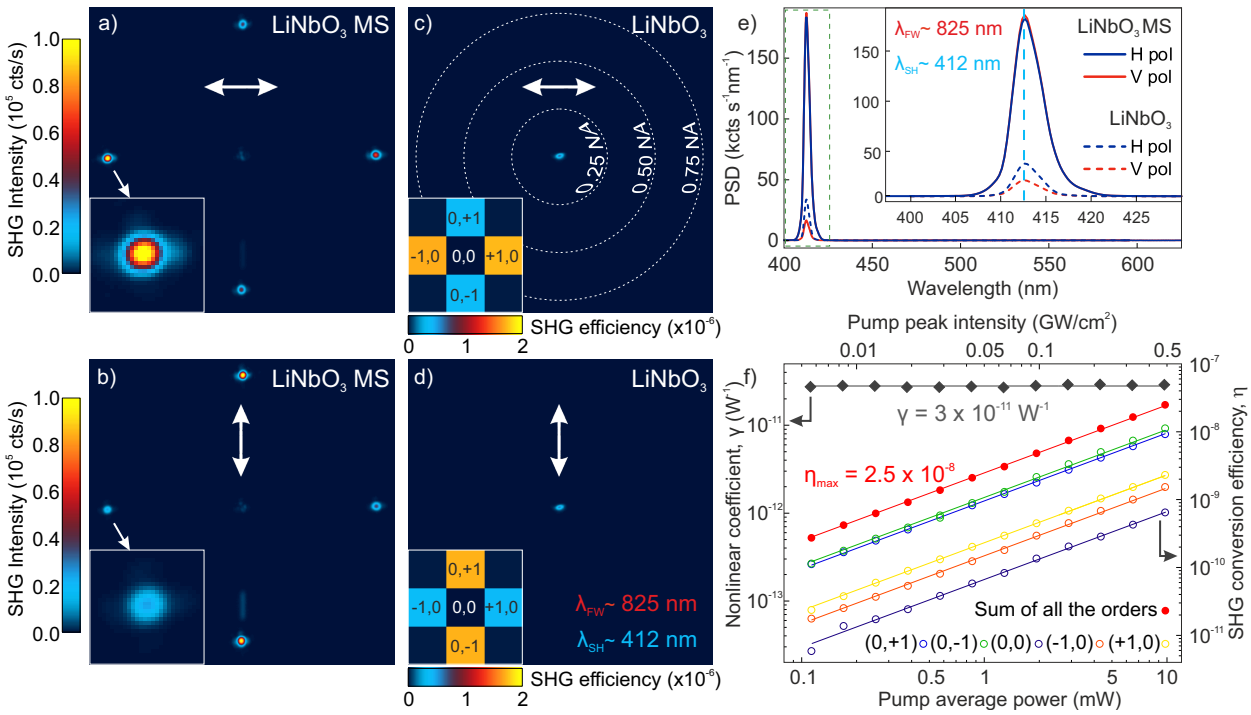

Figure 4: Nonlinear emission from the $LiNbO_3$ metasurface. a) BFP image of the SH emission from the optimized metasurface (MS) ($R = 175\,\text{nm}$, $P = 590\,\text{nm}$) excited with horizontal polarization. Inset: zoom of the (-1,0) diffraction order. b) BFP image of the same metasurface illuminated with vertical polarization. Inset: zoom of the (-1,0) diffraction order. c,d) BFP images acquired on the unpatterned $LiNbO_3$ using either horizontal (c) or (d) vertical excitation polarization. The FW employed to acquire the BFP maps and the corresponding SH are ∼825 nm and ∼412 nm, respectively. The insets of (c) and (d) are the simulated SHG intensities emitted by the metasurfaces in each diffraction order, for comparison with (a) and (b) respectively. e) (Solid lines) spectrum of the nonlinear emission by the metasurface under horizontal (blue) and vertical (red) exciting polarization, compared to the nonlinear emission by the unpatterned $LiNbO_3$ substrate (dashed lines). The input intensity is $0.5\,\text{GW/cm}^2$. f) SHG conversion efficiency of the diffraction orders as a function of the excitation intensity for vertical pump polarization as in (b). The straight lines are linear fits with slope 1.

confirm that the emission from the metasurface is pure SHG. Comparing the overall emission from the metasurface with that from the unpatterned $LiNbO_3$ film (see Figure 4e), one can note an order of magnitude emission enhancement by the metasurface. Even employing pump peak intensities below the GW cm^{-2} ($\sim 0.5\,\text{GW cm}^{-2}$), we obtained a SH emitted power $P_{\text{SH}} \sim 0.25\,\text{nW}$ from the metasurface, corresponding to $\eta \sim 2.5 \times 10^{-8}$ (see red dots Figure 4f). We also extrapolated the nonlinear coefficient $\gamma \equiv P_{\text{pk}}^{\text{SH}}/(P_{\text{pk}}^{\text{FW}})^2 \sim 3 \times 10^{-11}\,\text{W}^{-1}$ that, being a function of the SH ($P_{\text{pk}}^{\text{SH}}$) and FW ($P_{\text{pk}}^{\text{FW}}$) peak powers, allows assessing the non-

linear performances of the sample independently of the excitation source (*i. e.* pulse width and repetition rate). The nonlinear performances of the metasurface were also assessed via simulations using the approach described in the SI and in Ref. 22, and returned $\eta \sim 5 \times 10^{-6}$ and $\gamma \sim 5.8 \times 10^{-9}\,\mathrm{W}^{-1}$. These values are one order of magnitude higher than those numerically obtained from the bare $LiNbO_3$ film following the same approach, which is in excellent agreement with the enhancement found in the experiment. The two orders of magnitude difference between the measured and simulated conversion efficiencies can be ascribed to uncertainties in the estimation of the input intensity and of the optical transmittance of the detection path as well as to quantitative deviations of the numerical simulations from the experiments. For instance, while in the experiment excitation is provided by weakly focused ultrashort pulses (∼15 nm bandwidth), the simulation are performed using a monochromatic plane wave. It is also worth noting that the value of γ determined experimentally is in line with that of a recently reported $LiNbO_3$-based metasurface operating in the NIR.[24]

To assess the wavelength-dependent SHG behavior of the metasurface, we measured the SH power emitted into each diffraction order as a function of the FW using a fixed peak intensity of $\sim 0.33\,\mathrm{GW/cm^2}$, for either horizontal (Figure 5a) and vertical (Figure 5b) FW polarization. We found that the emission peaks at about 830 nm with a ∼50 nm spectral width of the metasurface resonance. Such spectral response reflects the major role played by the MD resonance in the nonlinear process, as also confirmed by the numerical simulations in Figure 5c and d. Both experiment and simulations confirm the presence of diffraction orders with polarization orthogonal to the pump polarization, which are up to four times weaker than the co-polarized ones and resonant to longer wavelengths. This behaviour is corroborated by the polarization-resolved polar plots of the SH emission collected for the two orthogonal pump polarization states (see Figure 5e–h), which indicate that the diffraction orders aligned with the pump are co-polarized with it while the orthogonal ones are cross-polarized. It is important to stress that the reported nonlinear diffraction sensibly differs from the linear one at the SH wavelength, where the impinging linearly-polarized

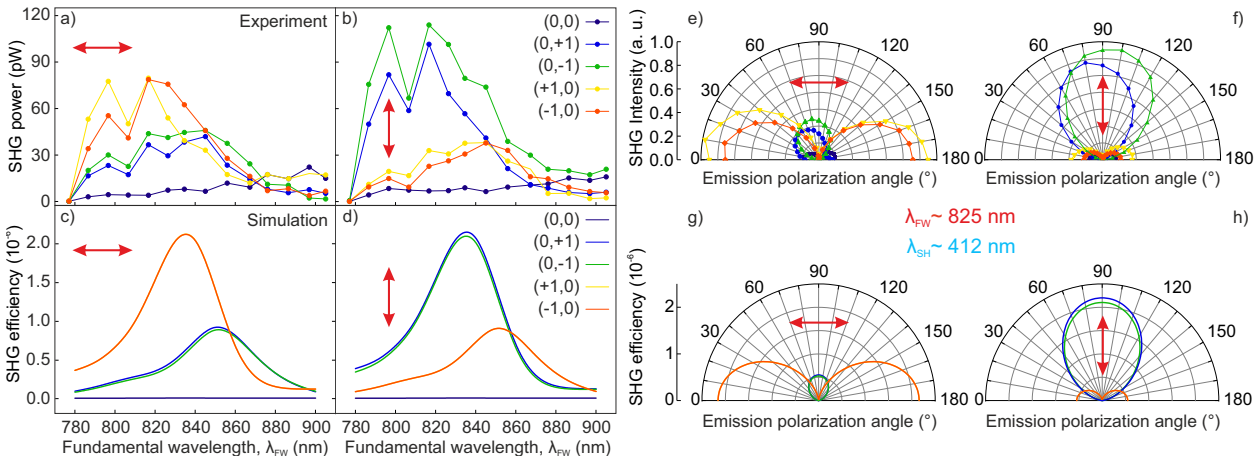

Figure 5: Wavelength-dependent SHG and polarized emission from the diffraction orders. a,b) Measured SH power for each diffraction order as a function of the FW for horizontal (a) and vertical (b) pump polarization. c,d) Simulated SHG efficiencies of each diffraction order as a function of the FW for the same configurations as in a) and b). e,f) Experimental polar plots showing the polarization state of the various diffraction orders for horizontal (e) and vertical (f) pump polarization. The FW employed to acquire the polar plots and the corresponding SH are ∼825 nm and ∼412 nm, respectively. g,h) Simulated polar plots corresponding to e) and f).

light is diffracted mainly into the modes lying in the polarization direction and preserving the polarization state. In the SHG process, the polarization switching between different diffraction orders is ascribed to the unevenly-distributed radial emission of the SH pattern of the individual meta-atoms, which originates from the interference between the nonlinearly excited MQ and the ED (see SI for details). The effective beaming of the in-plane field components of this radial mode in the respective diffraction orders endows the metasurface with its peculiar polarization and spectral selectivity. This adds another degree of freedom for controlling the SHG properties of our metasurface by engineering the emission of the individual meta-atom.

To conclude, we have designed and realized a $LiNbO_3$ nonlinear metasurface operating in the VIS range, featuring SHG performances in line with those of similar platforms[24] operating in the NIR (nonlinear coefficient $\gamma \approx 3 \times 10^{-11}\,\mathrm{W}^{-1}$) . In particular, thanks to the z-cut material and the metasurface periodicity, we observed a metasurface emission that is 10 times higher than that of the bare $LiNbO_3$ film. This emission is directed predominantly towards the diffraction orders, while the (0,0) order is further suppressed by a factor of 10 in the

metasurface. Therefore, our metasurface allows diffracting the SHG to the first diffraction orders modes with a signal two orders of magnitude stronger than the zeroth order, resulting in a $\sim$20 dB extinction ratio. Importantly, we report an intriguing polarization behaviour of the emitted SH, which is redirected by the metasurface preferentially in the diffraction orders that lie along the pump polarization. These diffraction orders are co-polarized with the pump polarization, whereas the ones laying in the direction orthogonal to it are cross-polarized. At resonance, the extinction ratio between the co- and cross-polarized diffraction orders is about four ($\sim$6 dB).

The possibility of efficient SH emission in the VIS range together with a polarization-controlled diffraction pattern make z-cut $LiNbO_3$ metasurfaces promising tools for nonlinear holography with polarization encoding, having potential applications *e. g.* in counterfeiting protection. Furthermore, the possibility for re-routing light with polarization selection could find further applications in free-space optical communications, such as Li-Fi.

Acknowledgement

The authors acknowledge financial support by the Italian Ministry of University and Research through the PRIN Project "NOMEN" (proj. 2017MP7F8F), the Australian Research Council (grant CE20010001) and by the European Commission through the H2020-FETOPEN project "METAFAST" (grant agreement no. 899673).

Supporting Information Available

This material is available free of charge via the internet at http://pubs.acs.org.

S.I: Experimental set-up. S.II: Fabrication of the metasurface S.III: Effect of the sample geometry. S.IV: SHG conversion efficiency and nonlinear parameter. S.V: Numerical simulations of the linear response. S.VI: Numerical simulations of the SHG. S.VII: Multipolar analysis of the SH response

References

(1) Rahmani, M. et al. Nonlinear frequency conversion in optical nanoantennas and metasurfaces: materials evolution and fabrication. *Opto-Electronic Advances* **2018**, *1*, 180021.

(2) De Angelis, C., Leo, G., Neshev, D. N., Eds. *Nonlinear Meta-Optics*; CRC Press, 2020.

(3) Pertsch, T.; Kivshar, Y. Nonlinear optics with resonant metasurfaces. *MRS Bull.* **2020**, *45*, 210–220.

(4) Shcherbakov, M. R.; Neshev, D. N.; Hopkins, B.; Shorokhov, A. S.; Staude, I.; Melik-Gaykazyan, E. V.; Decker, M.; Ezhov, A. A.; Miroshnichenko, A. E.; Brener, I.; Fedyanin, A. A.; Kivshar, Y. S. Enhanced Third-Harmonic Generation in Silicon Nanoparticles Driven by Magnetic Response. *Nano Lett.* **2014**, *14*, 6488–6492.

(5) Camacho-Morales, R. et al. Nonlinear Generation of Vector Beams from AlGaAs Nanoantennas. *Nano Lett.* **2016**, *16*, 7191–7197.

(6) Gili, V. F.; Carletti, L.; Locatelli, A.; Rocco, D.; Finazzi, M.; Ghirardini, L.; Favero, I.; Gomez, C.; Lemaître, A.; Celebrano, M.; De Angelis, C.; Leo, G. Monolithic AlGaAs second-harmonic nanoantennas. *Opt. Express* **2016**, *24*, 15965–15971.

(7) Liu, S.; Sinclair, M. B.; Saravi, S.; Keeler, G. A.; Yang, Y.; Reno, J.; Peake, G. M.; Setzpfandt, F.; Staude, I.; Pertsch, T.; Brener, I. Resonantly Enhanced Second-Harmonic Generation Using III–V Semiconductor All-Dielectric Metasurfaces. *Nano Lett.* **2016**, *16*, 5426–5432.

(8) Grinblat, G.; Li, Y.; Nielsen, M. P.; Oulton, R. F.; Maier, S. A. Enhanced third harmonic generation in single germanium nanodisks excited at the anapole mode. *Nano Lett.* **2016**, *16*, 4635–4640.

(9) Cambiasso, J.; Grinblat, G.; Li, Y.; Rakovich, A.; Cortés, E.; Maier, S. A. Bridging the Gap between Dielectric Nanophotonics and the Visible Regime with Effectively Lossless Gallium Phosphide Antennas. *Nano Lett.* **2017**, *17*, 1219–1225.

(10) Xu, L.; Zangeneh Kamali, K.; Huang, L.; Rahmani, M.; Smirnov, A.; Camacho-Morales, R.; Ma, Y.; Zhang, G.; Woolley, M.; Neshev, D.; Miroshnichenko, A. E. Dynamic Nonlinear Image Tuning through Magnetic Dipole Quasi-BIC Ultrathin Resonators. *Adv. Sci.* **2019**, 1802119.

(11) Vabishchevich, P. P.; Liu, S.; Sinclair, M. B.; Keeler, G. A.; Peake, G. M.; Brener, I. Enhanced Second-Harmonic Generation Using Broken Symmetry III-V Semiconductor Fano Metasurfaces. *ACS Photonics* **2018**, *5*, 1685–1690.

(12) Liu, Z.; Xu, Y.; Lin, Y.; Xiang, J.; Feng, T.; Cao, Q.; Li, J.; Lan, S.; Liu, J. High-Q Quasibound States in the Continuum for Nonlinear Metasurfaces. *Phys. Rev. Lett.* **2019**, *123*, 253901.

(13) Löchner, F.; Fedotova, A. N.; Liu, S.; Keeler, G. A.; Peake, G. M.; Saravi, S.; Shcherbakov, M. R.; Burger, S.; Fedyanin, A. A.; Brener, I.; Pertsch, T.; Setzpfandt, F.; Staude, I. Polarization-Dependent Second Harmonic Diffraction from Resonant GaAs Metasurfaces. *ACS Photonics* **2018**, *5*, 1786–1793.

(14) Wang, L.; Kruk, S.; Koshelev, K.; Kravchenko, I.; Luther-Davies, B.; Kivshar, Y. Nonlinear Wavefront Control with All-Dielectric Metasurfaces. *Nano Lett.* **2018**, *18*, 3978–3984.

(15) Reineke, B.; Sain, B.; Zhao, R.; Carletti, L.; Liu, B.; Huang, L.; De Angelis, C.; Zentgraf, T. Silicon Metasurfaces for Third Harmonic Geometric Phase Manipulation and Multiplexed Holography. *Nano Lett.* **2019**, *19*, 6585–6591.

(16) Marino, G.; Gigli, C.; Rocco, D.; Lemaître, A.; Favero, I.; De Angelis, C.; Leo, G.

Zero-Order Second Harmonic Generation from AlGaAs-on-Insulator Metasurfaces. *ACS Photonics* **2019**, *6*, 1226–1231.

(17) Kim, K. H.; Rim, W. S. Anapole Resonances Facilitated by High-Index Contrast between Substrate and Dielectric Nanodisk Enhance Vacuum Ultraviolet Generation. *ACS Photonics* **2018**, *5*, 4769–4775.

(18) Timpu, F.; Sendra, J.; Renaut, C.; Lang, L.; Timofeeva, M.; Buscaglia, M. T.; Buscaglia, V.; Grange, R. Lithium Niobate Nanocubes as Linear and Nonlinear Ultraviolet Mie Resonators. *ACS Photonics* **2019**, *6*, 545–552.

(19) Huang, Z.; Lu, H.; Xiong, H.; Li, Y.; Chen, H.; Qiu, W.; Guan, H.; Dong, J.; Zhu, W.; Yu, J.; Luo, Y.; Zhang, J.; Chen, Z. Fano resonance on nanostructured lithium niobate for highly efficient and tunable second harmonic generation. *Nanomaterials* **2019**, *9*, 69.

(20) Gao, B.; Ren, M.; Wu, W.; Hu, H.; Cai, W.; Xu, J. Lithium Niobate Metasurfaces. *Laser Photonics Rev.* **2019**, *13*, 1800312.

(21) Qiyu, Y.; Liu, Y.; Gan, X.; Fang, C.; Han, G.; Hao, Y. Nonlinear Bound States in the Continuum of Etchless Lithium Niobate Metasurfaces. *IEEE Photonics J.* **2020**, *12*, 1–9.

(22) Carletti, L.; Li, C.; Sautter, J.; Staude, I.; De Angelis, C.; Li, T.; Neshev, D. N. Second harmonic generation in monolithic lithium niobate metasurfaces. *Opt. Express* **2019**, *27*, 33391.

(23) Ma, J.; Xie, F.; Chen, W.; Chen, J.; Wu, W.; Liu, W.; Chen, Y.; Cai, W.; Ren, M.; Xu, J. Resonantly tunable second harmonic generation from lithium niobate metasurfaces. **2020**, arXiv:2002.06594.

(24) Fedotova, A.; Younesi, M.; Sautter, J.; Vaskin, A.; Löchner, F. J.; Steinert, M.; Geiss, R.; Pertsch, T.; Staude, I.; Setzpfandt, F. Second-harmonic generation in resonant nonlinear metasurfaces based on lithium niobate. *Nano Lett.* **2020**, *20*, 8608–8614.

(25) Huang, Z.; Wang, M.; Li, Y.; Shang, J.; Li, K.; Qiu, W.; Dong, J.; Guan, H.; Chen, Z.; Lu, H. Highly Efficient Second Harmonic Generation of Thin Film Lithium Niobate Nanograting near Bound States in the Continuum. **2020**, arXiv:2006.10908.

(26) Wang, C.; Zhang, M.; Chen, X.; Bertrand, M.; Shams-Ansari, A.; Chandrasekhar, S.; Winzer, P.; Lončar, M. Integrated lithium niobate electro-optic modulators operating at CMOS-compatible voltages. *Nature* **2018**, *562*, 101–104.

(27) Luke, K.; Kharel, P.; Reimer, C.; He, L.; Loncar, M.; Zhang, M. Wafer-scale low-loss lithium niobate photonic integrated circuits. *Opt. Express* **2020**, *28*, 24452.

(28) Li, G.; Wu, L.; Li, K. F.; Chen, S.; Schlickriede, C.; Xu, Z.; Huang, S.; Li, W.; Liu, Y.; Pun, E. Y. B.; Zentgraf, T.; Cheah, K. W.; Luo, Y.; Zhang, S. Nonlinear Metasurface for Simultaneous Control of Spin and Orbital Angular Momentum in Second Harmonic Generation. *Nano Lett.* **2017**, *17*, 7974–7979.

(29) Xu, L. et al. Forward and Backward Switching of Nonlinear Unidirectional Emission from GaAs Nanoantennas. *ACS Nano* **2020**, *14*, 1379–1389.

(30) Alaee, R.; Rockstuhl, C.; Fernandez-Corbaton, I. An electromagnetic multipole expansion beyond the long-wavelength approximation. *Opt. Commun.* **2018**, *407*, 17–21.

Graphical TOC Entry

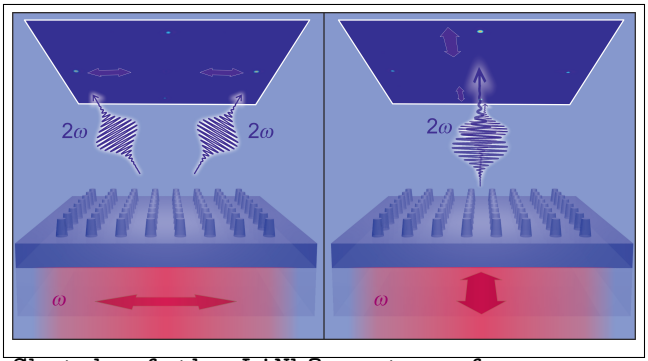

Sketch of the $LiNbO_3$ metasurface and its operation. Under linearly polarized excitation, the second harmonic is mostly emitted into the diffraction orders that lie along the pump direction, which are co-polarized with the pump. Thus rotating by 90° the pump polarization allows switching either of the two sets of orthogonal diffraction orders, as well as rotating the polarization of the nonlinear emission itself.